

# SIMULTANEOUS OBSERVATIONS OF SOLAR PLAGE WITH THE SOLAR EXTREME ULTRAVIOLET ROCKET TELESCOPE AND SPECTROGRAPH (SERTS), THE VLA, AND THE KITT PEAK MAGNETOGRAPH

JEFFREY W. BROSIUS,<sup>1</sup> JOSEPH M. DAVILA, WILLIAM T. THOMPSON,<sup>2</sup>  
 ROGER J. THOMAS, AND GORDON D. HOLMAN

Laboratory for Astronomy and Solar Physics, Code 682, NASA/Goddard Space Flight Center, Greenbelt, MD 20771<sup>3</sup>

N. GOPALSWAMY, STEPHEN M. WHITE, AND MUKUL R. KUNDU  
 Astronomy Program, University of Maryland, College Park, MD 20742

AND

HARRISON P. JONES

NASA/Goddard Space Flight Center, Southwest Solar Station, National Solar Observatory, Tucson, AZ 85726

Received 1992 October 23; accepted 1992 December 30

## ABSTRACT

We obtained simultaneous images of solar plage on 1991 May 7 with NASA/Goddard Space Flight Center's Solar Extreme Ultraviolet Rocket Telescope and Spectrograph (SERTS), the Very Large Array (VLA),<sup>4</sup> and the NASA/National Solar Observatory<sup>5</sup> spectromagnetograph at the NSO/Kitt Peak Vacuum Telescope. Using intensity ratios of Fe XVI to Fe XV emission lines, we find that the coronal plasma temperature is  $(2.3\text{--}2.9) \times 10^6$  K throughout the region. The column emission measure ranges from  $2.5 \times 10^{27}$  to  $1.3 \times 10^{28}$  cm<sup>-5</sup>. The calculated structure and intensity of the 20 cm wavelength thermal bremsstrahlung emission from the hot plasma observed by SERTS is quite similar to the observed structure and intensity of the 20 cm microwave emission observed by the VLA. Using the Meyer (1991, 1992) revised coronal iron abundance, we find no evidence either for cool absorbing plasma or for contributions from thermal gyroemission. Using the observed microwave polarization and the SERTS plasma parameters, we calculate a map of the coronal longitudinal magnetic field. The resulting values,  $\sim 30\text{--}60$  G, are comparable to extrapolated values of the potential field at heights of 5000 and 10,000 km.

*Subject headings:* Sun: corona — Sun: faculae, plages — Sun: magnetic fields — Sun: radio radiation — Sun: UV radiation

## 1. INTRODUCTION

Simultaneous observations of the Sun in the X-ray, EUV, optical, and microwave bands provide a wealth of information concerning the plasma and magnetic field in the solar corona. This information is vital to understanding processes such as coronal heating, solar wind acceleration, preflare energy storage, and active region evolution.

Using temperature-sensitive EUV or X-ray emission-line intensity ratios, the coronal plasma electron temperature can be determined. Combining this temperature with the emission-line intensity, the column emission measure can also be determined. These quantities are not only important by themselves, but are also essential ingredients for determining the coronal magnetic field strength. Because Zeeman splitting in coronal emission lines is undetectable, the Zeeman effect cannot be used for measuring the coronal magnetic field strength. Extrapolations of the coronal magnetic field using the mea-

sured photospheric magnetic field (obtained using the Zeeman effect) as a boundary condition can be done, but these depend upon certain extrapolation assumptions (e.g., potential, force-free), and are not actual measurements. A method for actually measuring the magnetic field strength in the solar corona is required. One such method is made possible by virtue of the dependence of the microwave emission upon the coronal magnetic field strength, and is accomplished by using the combined set of multiwaveband observations as described below.

Two emission mechanisms—thermal bremsstrahlung (free-free) and thermal gyroresonance (cyclotron)—contribute to the microwave emission from nonflaring coronal plasma. Thermal bremsstrahlung emission results from the interaction of unbound electrons with protons. The intensity of the thermal bremsstrahlung emission at any desired wavelength can be calculated from the coronal plasma temperature and column emission measure. This represents the minimum possible microwave intensity which emanates from the plasma. Thermal gyroemission results from thermal electrons spiraling along coronal magnetic field lines. It is emitted at low harmonics of the local electron gyrofrequency. A comparison of the calculated and the observed microwave intensities enables one to determine the dominant microwave emission mechanism.

Simultaneous observations in the X-ray, extreme-ultraviolet (EUV), optical, and microwave bands have been carried out since the *Skylab* era using a variety of instrumentation in each of these wave bands. In some cases it was concluded that thermal gyroemission was the dominant microwave emission mechanism, and the coronal magnetic field strength was deter-

<sup>1</sup> Also Hughes STX Corporation, 4400 Forbes Boulevard, Lanham, MD 20706.

<sup>2</sup> Also Applied Research Corporation, 8201 Corporate Drive, Landover, MD 20785.

<sup>3</sup> Postal address.

<sup>4</sup> The Very Large Array is a facility of the National Radio Astronomy Observatory, which is operated by Associated Universities, Inc., under cooperative agreement with the National Science Foundation.

<sup>5</sup> The National Solar Observatory is a Division of the National Optical Astronomy Observatories, which is operated by the Association of Universities for Research in Astronomy, Inc., under cooperative agreement with the National Science Foundation.

mined by establishing which harmonic of the local electron gyrofrequency was the dominant one (Kundu, Schmahl, & Gerassimenko 1980; Kundu, Schmahl, & Rao 1981; Pallavicini, Sakurai, & Vaiana 1981; Shibasaki et al. 1983; Webb et al. 1983; Webb et al. 1987; Lang et al. 1987b; Brosius et al. 1992). This can be done quite reliably for active region loops and sunspots by comparing the observed intensity and polarization structure with theoretical models (Holman & Kundu 1985; Brosius & Holman 1988, 1989).

Frequently, the observed microwave intensity has been found to be less (by factors of 2–5) than the thermal bremsstrahlung (minimum possible) intensity calculated from the X-ray or EUV observations. This has been interpreted as evidence for the presence of relatively cool absorbing plasma along the line of sight between the observer and the microwave-emitting region (Holman 1986; Webb et al. 1987; Lang et al. 1987a; Nitta et al. 1991; Brosius, Holman, & Schmelz 1991; Brosius et al. 1992; Schmelz et al. 1992). Additional evidence for the presence of such cool material, deduced from different types of observations, has been presented by Schmahl & Orrall (1979) and Kanno & Suematsu (1982).

For the present study we obtained simultaneous observations of solar plage on 1991 May 7 with the NASA/Goddard Space Flight Center (GSFC) Solar EUV Rocket Telescope and Spectrograph (SERTS), the Very Large Array (VLA), and the NASA/National Solar Observatory (NSO) spectromagnetograph. In § 2 we describe the observations and analysis of the individual data sets obtained with each of the instruments, in § 3 we discuss the results of the analysis of the combined data set, and in § 4 we emphasize our conclusions from this study.

## 2. OBSERVATIONS AND DATA ANALYSIS

### 2.1. SERTS Observations

The SERTS imaging spectrograph is described by Neupert et al. (1992b). The instrument was designed so that (1) it retained the stigmatic imaging capability of the NRL SO 82A spectroheliograph on *Skylab* (Tousey et al. 1977) while reducing image overlap in spectral regions with numerous emission lines, and (2) it provided high spectral resolution with less spatial convolution than had been available with earlier instruments. The SERTS design achieves these objectives by introducing an imaging fore-optic with its image plane at the entrance aperture of a toroidal grating spectrograph so that either spectra or spectroheliograms with high spatial selectivity can be obtained, depending on the configuration of the entrance aperture. In fact, the actual spectrograph entrance aperture enables both spectra and spectroheliograms to be obtained simultaneously. Spectra are obtained along a narrow 4:9 long slit connecting two rectangular lobes within which the spectroheliograms are imaged. The upper lobe covers a  $4.8 \times 8.2$  area on the Sun, and the lower one covers a  $4.8 \times 7.6$  area. The spatial resolution is  $\sim 7''$ , and the spectral resolution is less than  $75 \text{ m}\text{\AA}$ . By adjusting the pointing of the instrument during its flight, both images and spectra can be obtained for the same portion of the Sun. The degree of image overlap for adjacent spectral lines in the lobes is only about one-sixth that of the spectrograph design employed by the NRL SO 82A instrument on *Skylab*. Some results from a previous flight of the instrument (1989 May 5) are given by Neupert et al. (1992a), Thompson et al. (1993), and Jordan et al. (1993).

SERTS was launched on a Terrier-boosted Black Brant rocket from White Sands, New Mexico, at 1805 UT on 1991

May 7. It reached a maximum altitude of 327 km, and acquired spectrographic data from 1806 to 1813 UT. This was the first flight of a multilayer coated diffraction grating (Davila et al. 1992; Keski-Kuha, Thomas, & Davila 1992). The multilayer coating improved the grating efficiency by factors up to 9 over a fairly wide portion of our spectral range (Thomas et al. 1991). The instrument performed well, and we obtained spectra and spectroheliograms in the spectral range 235–450 Å. In the first of two pointing positions, we obtained spectroheliograms of AR 6615 (S10 W30, in the upper lobe) and of off-limb areas (in the lower lobe), and spectra of the quiet Sun between them. In the second pointing position, we obtained spectroheliograms of plage (N11 W10, in the upper lobe) and of AR 6608 (S22 W63, in the lower lobe), and spectra of AR 6615. No spectra were obtained for the plage. For each pointing position we obtained images at four different exposure times to ensure the availability of optimally exposed images and spectra for emission lines covering a wide range of intensities. The images were recorded on Eastman Kodak 101-07 EUV-sensitive photographic film, and digitized with a Perkin-Elmer microdensitometer.

Photometric EUV calibrations for each optical component were carried out either at GSFC or at the Synchrotron Ultraviolet Radiation Facility (SURF II) of the National Institute of Standards and Technology. The film's  $D \log E$  relation was derived from ratios of flight images with differing exposure times. Corrections for the effects of atmospheric extinction at rocket altitudes were made for each exposure and incorporated into our calculations of the film response and overall instrumental sensitivity. The resulting relative calibration was verified by comparing flight observations of active region spectral line pairs whose intensity ratios are known to be density- and temperature-insensitive (Neupert & Kastner 1983). Including all correction factors, we estimate that relative line intensities are accurate to better than 20% at wavelengths above 300 Å, and perhaps somewhat worse at wavelengths below 300 Å. The absolute photometric scale, accurate to better than a factor of 2, was derived by fitting our solar observations to reported values for the average He II quiet-Sun intensity at 304 Å. The uncertainty in the absolute photometric scale means that derived column emission measures are uncertain by factors approaching 2. Details of the SERTS calibration procedures are given by Thomas, Neupert, & Thompson (1992).

In this paper we concentrate on the plage located northeast of AR 6615. This area was associated with a small  $\alpha$  sunspot, although it was never assigned an independent active region number. No spectra were obtained for this relatively weak region, but images were obtained for the following emission lines, where the numbers in parentheses correspond to the measured wavelength in angstroms and the temperature of maximum relative ion abundance in kelvins: He II (303.78,  $5.0 \times 10^4$ ), Mg IX (368.07,  $1.0 \times 10^6$ ), Fe XV (284.16 and 417.24,  $2.0 \times 10^6$ ), and Fe XVI (335.40 and 360.75,  $2.5 \times 10^6$ ). Images for additional wavelengths are in principle available, but those just listed have the minimum contamination from adjacent lines.

The SERTS spectroheliograms were coaligned with the ground-based observations by matching features common to both the SERTS He II 304 Å image and the Kitt Peak He I 10830 Å image. To account for solar rotation, the Kitt Peak images were rotated to the time of the SERTS flight. In the  $4.8 \times 8.2$  SERTS image, at least 13 He II features were found to have a He I counterpart. Using a least-squares fitting routine,



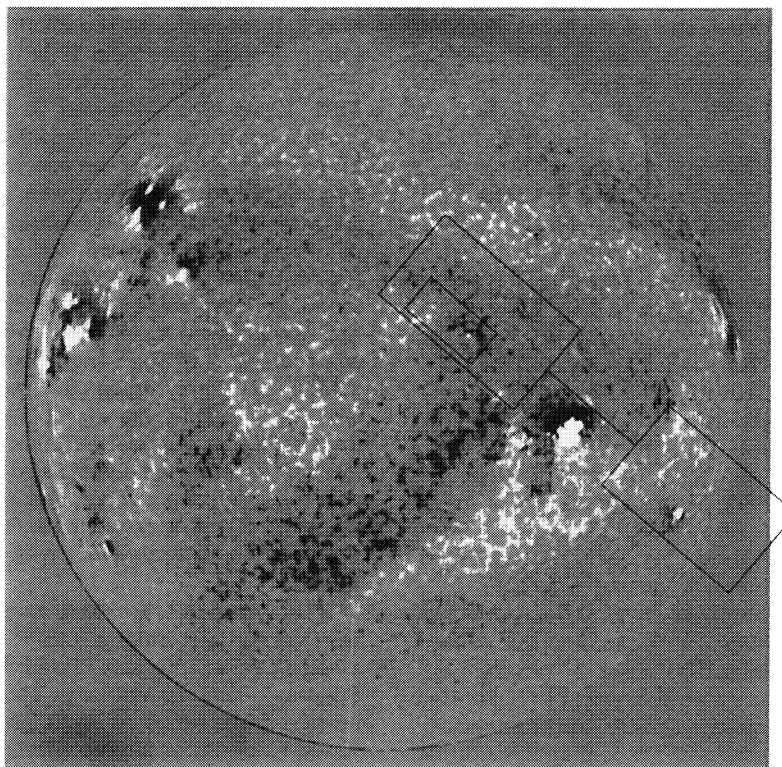


FIG. 1.—Pointing of the SERTS imaging spectrograph during the flight of 1991 May 7. The lobes and slit are shown on the full-disk Kitt Peak magnetogram. In this pointing position the slit crossed the edge of AR 6615, and the upper lobe obtained the images used for analysis in this paper. The small rectangle inside the upper lobe shows the area selected for analysis. Spectroheliograms of this area, measuring  $1'.77 \times 3'.83$ , are shown in Fig. 2. Solar north is at the top.

the necessary coalignment parameters were found: the orientation angle of the SERTS image relative to solar north, the coordinates of the lower left-hand corner of the SERTS image relative to Sun center, and the SERTS image scale. The SERTS image scale obtained in this way is in excellent agreement with its design value. Because the absolute pointing of the VLA is known to high accuracy, its pointing relative to Kitt Peak can easily be determined, so that the coalignment of the SERTS images relative to Kitt Peak images yields a mutually coaligned data set. The formal uncertainty in the coalignment is

$\sim 10''$ . Figure 1 shows the pointing of the SERTS instrument on the full-disk Kitt Peak magnetogram.

In Figure 2 we show intensity maps of the plage in the six selected EUV emission lines. These images,  $1'.77 \times 3'.83$ , are closeups of the region, and do not correspond to the full upper lobe. In Table 1 we list the average, maximum, and minimum intensities in each of the images in Figure 2. Notice that the ratio of the intensities of the Fe xvii lines at 361 and 335 Å is 0.51 (with a standard deviation of 0.055), in excellent agreement with the theoretical value of 0.48. The ratio of the inten-

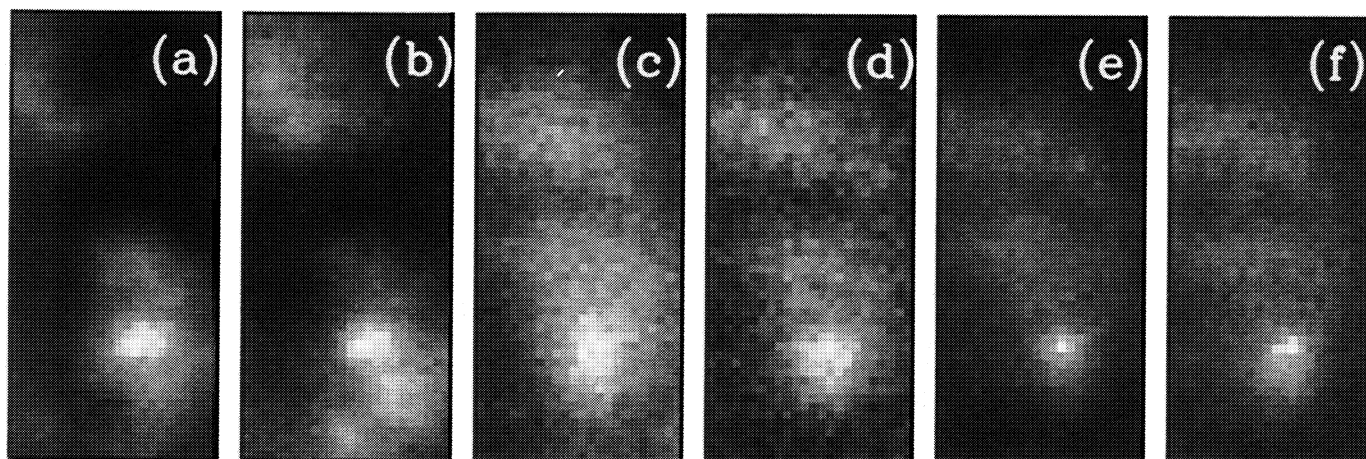


FIG. 2.—Spectroheliograms of the plage region in six prominent emission lines: (a) He II at 304 Å; (b) Mg IX at 368 Å; Fe xv at (c) 284 Å and (d) 417 Å; and Fe xvii at (e) 335 Å and (f) 361 Å. All images appear to be of comparable brightness because they are all scaled individually. See Table 1 for a list of the actual individual intensities. The pixel size in these and the following figures is  $4''.42 \times 4''.42$ .

TABLE 1  
INTENSITIES OF PLAGE EMISSION LINES (ergs cm<sup>-2</sup> s<sup>-1</sup> sr<sup>-1</sup>)

Image	$I_{\text{avg}}$	$I_{\text{min}}$	$I_{\text{max}}$
He II 304 Å .....	$9.63 \times 10^3$	$4.20 \times 10^3$	$2.67 \times 10^4$
Mg IX 368 Å .....	$1.14 \times 10^3$	$5.77 \times 10^2$	$2.44 \times 10^3$
Fe XV 284 Å .....	$8.53 \times 10^3$	$4.60 \times 10^3$	$1.39 \times 10^4$
Fe XV 417 Å .....	$3.17 \times 10^2$	$1.72 \times 10^2$	$5.69 \times 10^2$
Fe XVI 335 Å .....	$4.45 \times 10^3$	$1.93 \times 10^3$	$1.09 \times 10^4$
Fe XVI 361 Å .....	$2.27 \times 10^3$	$1.02 \times 10^3$	$5.00 \times 10^3$

sities of the Fe xv lines at 417 and 284 Å is 0.037 ( $\sigma = 0.003$ ), also in good agreement with the theoretical value of 0.034. Such tests of the instrument's relative calibration suggest that it can provide reliable determinations of temperatures and emission measures for the observed plage region.

The rates of emission per unit volume for numerous collisionally excited ionic emission lines have been calculated by Stern, Wang, & Bowyer (1978) and Landini & Monsignori Fossi (1990). Using their procedure, we obtain the following expression for the intensity ratio of two lines which are formed by radiative de-excitation to the ground level following collisional excitation from the ground level to the upper level:

$$\frac{I_a}{I_b} = \frac{f_a}{f_b} \frac{G_a}{G_b} \left( \frac{n_{i,a}}{n_E} \right) \left( \frac{n_{i,b}}{n_E} \right)^{-1} \exp \left( \frac{E_b - E_a}{kT_e} \right). \quad (1)$$

$I_\lambda$  is the intensity at wavelength  $\lambda$ ,  $f_\lambda$  is the oscillator strength,  $G_\lambda$  is the Gaunt factor (calculated according to Landini & Monsignori Fossi 1990 and Mewe, Gronenschild, & van den Oord 1985),  $n_{i,\lambda}/n_E$  is the relative ion abundance,  $E_\lambda$  is the energy of the transition,  $k$  is Boltzmann's constant, and  $T_e$  is the temperature. The temperature can be determined from the intensity ratio if the relative ion abundances are known as functions of temperature.

For our analysis, we use the intensity ratios of Fe xvi (Fe<sup>+15</sup>) at 335 Å to Fe xv (Fe<sup>+14</sup>) at 284 Å (two wavelengths which are in the bandpass enhanced by the multilayer coating), and Fe xvi at 361 Å to Fe xv at 284 Å. Both of these intensity ratios vary by factors  $\sim 390$  over the range  $6.1 \leq \log T_e \leq 6.9$ . The ratio  $I_{335}/I_{284}$  is 0.022 at  $\log T_e = 6.1$ , 1.1 at  $\log T_e = 6.5$ , and 8.6 at  $\log T_e = 6.9$ . This strong temperature dependence makes the ratios relatively insensitive to uncertainties such as photometric calibration or errors in the atomic parameters (Nitta et al. 1991). Using  $f_{284} = 0.827$ ,  $f_{335} = 0.270$ ,  $f_{361} = 0.125$  (Fuhr, Martin, & Wiese 1988) and the ionization equilibrium calculations of Arnaud & Raymond (1992), we find

$$\log T_e = 5.783 + 0.710 \left( \frac{I_{335}}{I_{284}} \right)^{0.212} \quad (2)$$

and

$$\log T_e = 5.789 + 0.827 \left( \frac{I_{361}}{I_{284}} \right)^{0.215} \quad (3)$$

for  $6.1 \leq \log T_e \leq 6.9$ . These yield temperatures of  $(2.52 \pm 0.16) \times 10^6$  and  $(2.58 \pm 0.16) \times 10^6$  K, respectively, when the ratios of the average intensities in Table 1 are used. Error bars are based on the 20% uncertainty in the relative line intensities.

The column emission measure (EM =  $\int N_e^2 dl$ , where  $N_e$  is the electron number density and  $dl$  is an element of path length along the line of sight) can be derived from the rate of emission per unit volume (Landini & Monsignori Fossi 1990; Stern et

al. 1978; Pottasch 1963, 1964) and the observed line intensity. We obtain

$$\int N_e^2 dl = 5.755 \times 10^{18} I_\lambda T_6^{1/2} \left( \frac{n_i}{n_E} \right)^{-1} \left( \frac{n_E}{n_H} \right)^{-1} f^{-1} G^{-1} \times \exp \left( \frac{143.9}{\lambda T_6} \right) \quad (4)$$

for cases in which the branching ratio is 1 (which it is for the lines that we use in this analysis; see, e.g., Stern et al. 1978).  $I_\lambda$  is the observed intensity in ergs cm<sup>-2</sup> s<sup>-1</sup> sr<sup>-1</sup>,  $T_6$  is the electron temperature in 10<sup>6</sup> K,  $n_i/n_E$  is the abundance of the relevant ion with respect to the total element abundance ( $n_i$  is the number density of the relevant ion, and  $n_E$  is the number density of the relevant element),  $n_E/n_H$  is the element abundance with respect to hydrogen ( $n_H$  is the hydrogen number density),  $f$  is the oscillator strength,  $G$  is the Gaunt factor, and  $\lambda$  is the wavelength in angstroms. Using the revised Meyer (1985, 1991, 1992) coronal iron abundance of  $1.33 \times 10^{-4}$ , the average electron temperature of  $2.52 \times 10^6$  K derived using equation (2) above, the average Fe xvi 335 Å intensity from Table 1, the relative ion abundance of 0.269 at  $\log T = 6.4$  from Arnaud & Raymond (1992), an oscillator strength of 0.270, and a Gaunt factor of 1.04, we obtain an average column emission measure of  $4.80 \times 10^{27}$  cm<sup>-5</sup>. (Accounting for the uncertainty in the absolute photometric scale, the maximum value for the average column emission measure is  $9.60 \times 10^{27}$  cm<sup>-5</sup>, and the minimum value is  $2.40 \times 10^{27}$  cm<sup>-5</sup>.)

By taking the ratio of the Fe xvi 335 Å map to the Fe xv 284 Å map, a temperature map for the entire region is obtained. This map has a maximum value of  $2.89 \times 10^6$  K (where oppositely directed magnetic field polarities are closely spaced; see below) and a minimum value of  $2.26 \times 10^6$  K (toward the edges of the region). Over most of the plage, the temperature remains near  $2.5 \times 10^6$  K. Because the temperature map is essentially featureless, it is not shown here. By inserting the temperature map and one of the EUV intensity maps used to obtain this temperature map in equation (4), a map of the column emission measure is obtained. This map closely resembles the Fe xv and Fe xvi intensity maps. The emission measure ranges from  $2.46 \times 10^{27}$  to  $1.28 \times 10^{28}$  cm<sup>-5</sup> and is shown in Figure 3a. The temperature and emission measure maps are discussed further in § 3, where they are used in more detailed analysis of the combined data set. The ratio of the Fe xvi 361 Å map to the Fe xv 284 Å map yields similar values for the temperature and emission measure, with maximum and minimum temperature values of  $2.88 \times 10^6$  and  $2.31 \times 10^6$  K, and column emission measure ranging from  $2.55 \times 10^{27}$  to  $1.23 \times 10^{28}$  cm<sup>-5</sup>.

## 2.2. Kitt Peak Magnetogram

The NASA/NSO spectromagnetograph (Jones et al. 1992) was used to obtain a full-disk photospheric longitudinal magnetogram between 1536 and 1626 UT, and a full-disk He I 10830 Å image between 1640 and 1722 UT. The fluxes have been appropriately calibrated so that reliable longitudinal magnetic field strengths (uncertainties  $\lesssim 5\%$ ) are obtained. The instrumental resolution is  $\sim 2''$ , and the data are digitized in 1'077 pixels. The Kitt Peak images have been warped using a solar rotation routine to correspond to the time of the rocket flight. The magnetogram for the plage region analyzed in this paper is shown in Figure 3b. The maximum outward-directed



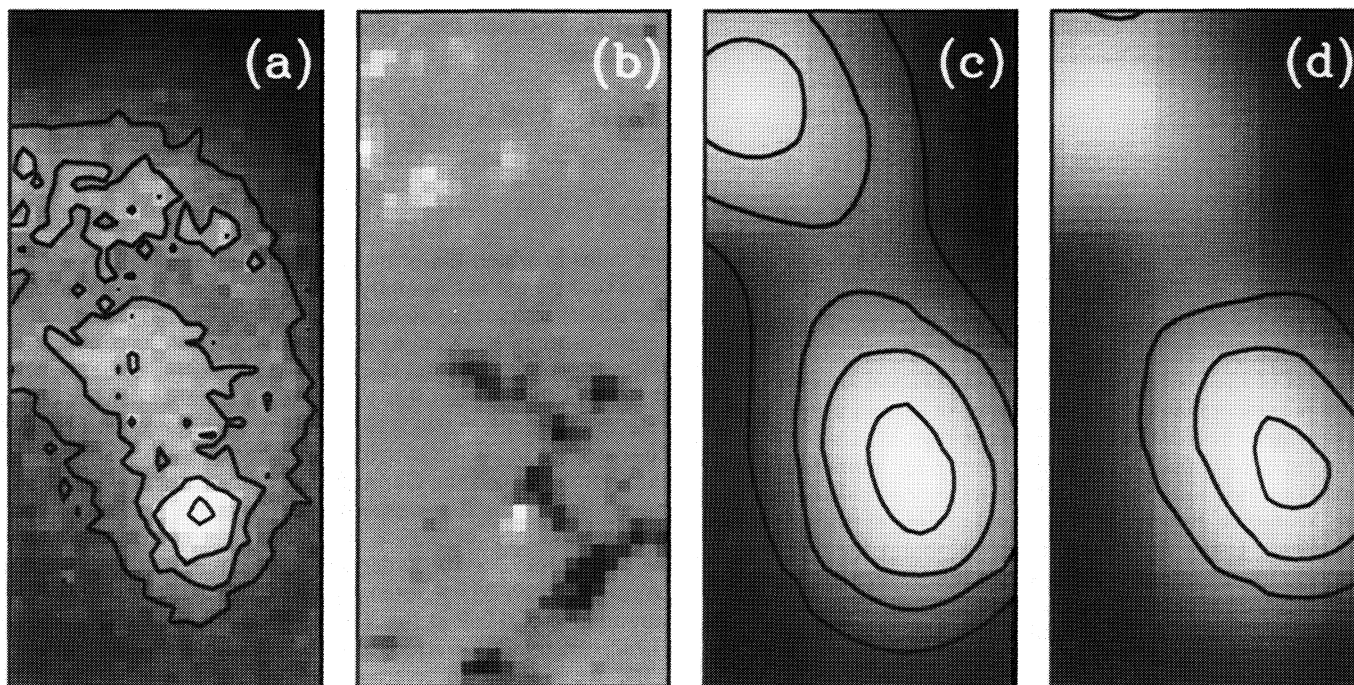


FIG. 3.—(a) Column emission measure calculated from the SERTS observations. The contour levels are  $0.5, 0.6, 0.7$ , and  $1.0 \times 10^{28} \text{ cm}^{-5}$ . The field of view and image orientation is the same as in Fig. 2. (b) Kitt Peak photospheric longitudinal magnetogram. White represents outward-directed (positive) field, and black represents inward-directed (negative) field. (c) VLA 20 cm intensity ( $I$ ) gray-scale image with  $I$  contours superposed. The contour levels are  $1.5, 2.0, 2.5$ , and  $3.0 \times 10^5 \text{ K}$ . A quiet-Sun background brightness temperature of  $1.0 \times 10^5 \text{ K}$  has been added to the measured intensities. (d) VLA 20 cm  $I$  gray-scale image with circular polarization ( $V$ ) contours superposed. The  $V$  contour levels are  $-0.2, -0.4$ , and  $-0.6 \times 10^5 \text{ K}$ .

field in this region is 621 G, and the maximum inward-directed field is 571 G. Regions of strong positive and negative polarity lie in close proximity in the lower central portion of Figure 3b. Both the temperature and the emission measure calculated from the SERTS observations peak at this location. It should also be pointed out that the positive polarity component of these closely spaced opposite magnetic polarities represents emerging magnetic flux, as it was not present in magnetograms obtained on the three preceding days.

A filament channel straddles the neutral line separating the two main regions of opposite magnetic polarity (roughly dividing the images of Figs. 2 and 3 into a top half and a bottom half). This channel appears as an intensity depression in both the EUV and the microwave intensity. Since, as described above, the electron temperature was found to be relatively constant across the region, the filament channel intensity depression cannot be attributed to a temperature decrease. It must, therefore, be attributed to the diminished column emission measure in the channel (see Fig. 3a).

### 2.3. VLA Observations

The VLA was in D-configuration and provided sufficiently good  $uv$  coverage to map the large-scale features of the Sun. Observations were made in the 20, 6, 3.2, and 2 cm wave bands between 1411 and 2010 UT. At 20 cm wavelength the field of view covers the whole Sun, so that all of the disk regions observed by SERTS were also observed at 20 cm wavelength. In the shorter wavelength bands, only AR 6615 and AR 6608 were observed. Because of nonavailability of suitable phase calibrators, 3C 48 was used as both flux and phase calibrator. The array spent 2–3 minutes on each solar source, with a 3 s time integration. Maps were made separately in the left-hand (L) and the right-hand (R) modes of circular polarization,

cleaned, and self-calibrated to correct for amplitude and phase errors. The final R and L maps were combined to make total intensity (Stokes  $I$ ) and circular polarization (Stokes  $V$ ) maps. These 20 cm maps of the plage are shown in Figures 3c and 3d. A quiet-Sun background brightness temperature of  $1 \times 10^5 \text{ K}$ , to which these observations are not sensitive because of its large spatial scale, has been added to the values in the total intensity map. The beam size for the 20 cm observations is  $53'' \times 45''$ .

The microwave intensities of the R and L components are commonly given in terms of brightness temperature (in K). The brightness temperature is the blackbody temperature corresponding to the measured flux density at the observed microwave wavelength. For an optically thick source, the brightness temperature of the emerging radiation is equal to the electron temperature of the source. The brightness temperature of the right-hand circularly polarized component is written as  $T_B^R$ , and that of the left-hand circularly polarized component is  $T_B^L$ . Total intensity (Stokes  $I$ ) is  $\frac{1}{2}(T_B^R + T_B^L)$ , and the degree of circular polarization (Stokes  $V$ ) is  $\frac{1}{2}(T_B^R - T_B^L)$ . The fractional polarization,  $P$ , is given by  $V/I$ .

The VLA observed the plage at a frequency of 1.446 GHz in the 20 cm wave band. The plage was not observed at any of the other wavelengths. The intensity shows a two-peaked structure, one peak on each side of the filament channel, with a weak bridge of emission connecting the two. The total intensity is highest on the side with the highest magnetic field strengths, which is also the side with two closely spaced patches of opposite magnetic polarity. The magnetic field strength is predominantly inward-directed on this side, and the emission is dominated by the left-hand circularly polarized component. The maximum fractional polarization is  $\sim -0.22$ , and the maximum total intensity on this side of the filament channel is



$3.25 \times 10^5$  K. On the other side of the filament channel, the magnetic field is predominantly outward-directed, and the maximum total intensity is  $2.80 \times 10^5$  K. The polarization on this side is dominated by the right-hand component, but is too weak to be reliable. The average 20 cm microwave brightness temperature over the plage area observed by SERTS (the frames shown in Fig. 2) is  $1.85 \times 10^5$  K.

### 3. RESULTS

The electron temperature and column emission measure obtained from the EUV data can be used to compute the thermal bremsstrahlung microwave emission from the EUV-emitting plasma. The optical depth due to thermal bremsstrahlung (free-free) absorption is (e.g., Lang 1980)

$$\tau_{ff}^{X,O} = \frac{9.786 \times 10^{-21} (\text{EM}) \ln(47T_e/\nu)}{n_\nu T_e^{1.5} (\nu \mp \nu_B \cos \theta)^2} = \tau_0 \left( 1 \mp \frac{\nu_B}{\nu} \cos \theta \right)^{-2}, \quad (5)$$

where  $T_e$  is the electron temperature in K, EM is the emission measure in  $\text{cm}^{-5}$ ,  $\nu$  is the observation frequency in GHz,  $n_\nu$  is the index of refraction ( $\sim 1$  for plasma and field conditions here),  $\nu_B$  is the electron gyrofrequency ( $\nu_B = 2.8 \times 10^{-3} B$ , where  $B$  is in gauss and  $\nu_B$  is in gigahertz),  $\theta$  is the angle between the field and the line of sight,  $\tau_0$  is the optical depth of the unmagnetized plasma, and the minus sign refers to the  $X$ -mode, while the plus sign refers to the  $O$ -mode. The thermal bremsstrahlung brightness temperature predicted for each mode can be calculated using

$$T_{B;X,O}^{\text{pred}} = T_e [1 - \exp(-\tau_{ff}^{X,O})]. \quad (6)$$

In a magnetized plasma, the optical depth, and hence the predicted brightness temperature, of the  $X$ -mode emission is expected to be higher than that of the  $O$ -mode. If the longitudinal (line-of-sight) magnetic field component in the microwave emission region is directed toward the observer (outward-directed, or positive field), then the  $X$ -mode corresponds to the R component, while the  $O$ -mode corresponds to the L component. If the longitudinal magnetic field component is directed away from the observer, then the  $X$ -mode corresponds to the L component and the  $O$ -mode corresponds to the R component. The predicted total intensity  $I^{\text{pred}}$  is simply the average brightness temperature of the two modes.

Assuming initially that the plasma observed by SERTS was unmagnetized (an assumption which does not affect the calculated total intensity  $I^{\text{pred}}$ ), and using the average temperature ( $2.52 \times 10^6$  K) and emission measure ( $4.80 \times 10^{27} \text{ cm}^{-5}$ ) values obtained in § 2.1, we calculate an average 20 cm opacity of 0.102 and an average 20 cm predicted total intensity of  $2.45 \times 10^5$  K. This is a factor of only 1.32 greater than the observed total intensity averaged over the same region. Thus the averaged 20 cm thermal bremsstrahlung intensity calculated using the plasma parameters obtained with SERTS is comparable to that observed with the VLA. (Recall that the SERTS absolute intensity calibration is uncertain by a factor approaching 2. This produces a factor of 2 uncertainty in the calculated optical depth, and hence a factor of 2 or less uncertainty in the predicted total intensity.)

By inserting the temperature and emission measure from corresponding map pixels into equations (5) and (6), a map of the predicted total intensity (at the 1.446 GHz observation frequency) is obtained. Initially we assume an unmagnetized coronal plasma, but we will later evaluate the coronal longitudinal

magnetic field using the combined SERTS and VLA observations. The predicted 20 cm total intensity map is shown (superposed on the magnetogram) in Figure 4a. This map was generated by using the temperature calculated from the  $I_{335}/I_{284}$  ratio, and the corresponding emission measure calculated from the Fe XVI 335 Å intensity. It has been smoothed over 9 pixels in each dimension to compensate for the fact that the VLA beamwidth is nearly an order of magnitude larger than the SERTS pixel size. The corresponding observed 20 cm total intensity map is shown in Figure 4b. Notice that the overall structure of the predicted and the observed maps is similar: two main emission peaks separated by an intensity depression corresponding to the filament channel. (This channel appears dark in the EUV and microwave bands, not because the temperature is lower there but because the emission measure is lower there.) The predicted and observed brightness temperatures are equal, to within the error bars. In Figure 4c we show the ratio of the predicted to the observed brightness temperatures. Notice that over most of the region, the predicted and the observed brightness temperatures are equal to better than 50%. Thus, because the thermal bremsstrahlung emission calculated for the hot coronal plasma observed by SERTS yields both the structure and the brightness temperature observed with the VLA, we conclude that thermal bremsstrahlung from this hot plasma alone is the mechanism responsible for the observed microwave emission. Neither cool absorbing plasma nor magnetic fields sufficient to produce gyroemission are required in the corona over the plage. This is consistent with the results of Chiuderi-Drago et al. (1982), who find that the plage temperature and emission measure inferred from X-ray emission lines yield 20 cm thermal bremsstrahlung brightness temperatures which agree with the observed values.

We can gain quantitative information on the magnetic fields in the corona by using the radio polarization data as well. Combining the plasma parameters obtained using SERTS with the microwave polarization obtained using the VLA, we have calculated a map of the coronal longitudinal magnetic field  $B_z$  ( $B_z = B \cos \theta$ ; see equation [5]). This is possible because of the dependence of the thermal bremsstrahlung optical depth upon the coronal magnetic field. Inserting equation (5) (for each mode) in equation (6), and relating the observed polarization  $P$  ( $P = V^{\text{obs}}/I^{\text{obs}}$ ) to  $(T_{B;X}^{\text{pred}} - T_{B;O}^{\text{pred}})/(T_{B;X}^{\text{pred}} + T_{B;O}^{\text{pred}})$ , we obtain

$$B_z = 258P[1 - \exp(-\tau_0)]/[\tau_0 \exp(-\tau_0)]. \quad (7)$$

We assume in this derivation that  $B_z \leq 100$  G. This is likely to be a valid assumption, since the photospheric fields are relatively weak, and we have already seen that gyroresonance opacity, which would require fields of 180 G (third harmonic) or 130 G (fourth harmonic) in the corona, is not required. A map of the coronal longitudinal magnetic field calculated in this way is shown in Figure 5a. Careful attention has been given to relating each mode of circular polarization (R or L) to its appropriate mode of propagation ( $X$  or  $O$ ) to obtain the sign of the magnetic field in the microwave emission region. Contours are displayed only for areas in which the observed fractional polarization exceeds 0.05; values outside these areas are not reliable.

For comparison we show maps of the extrapolated coronal potential longitudinal magnetic field at heights of 5000 km (Fig. 5b) and 10,000 km (Fig. 5c). These were obtained using the Sakurai (1982) code. The contour levels in all three figures are



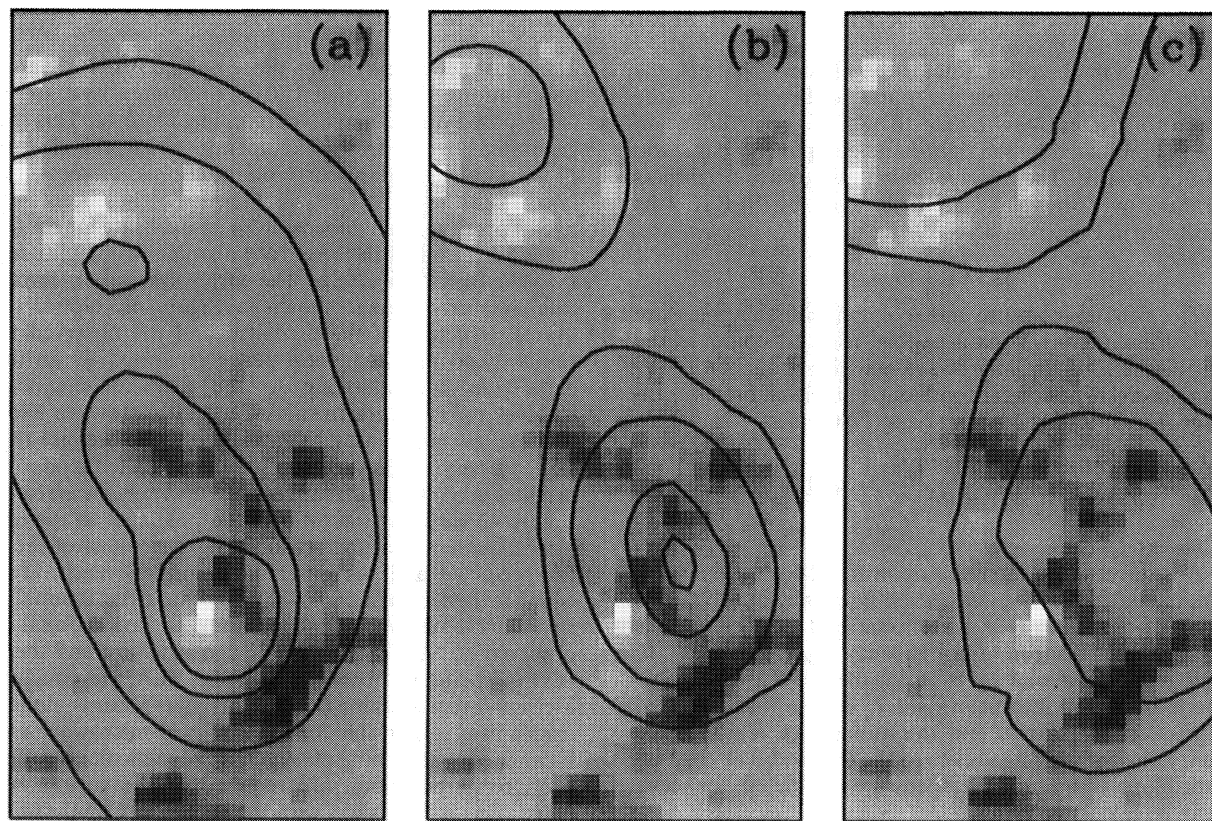


FIG. 4.—(a) Predicted and (b) observed 20 cm  $I$  contours on Kitt Peak magnetogram. Contour levels are  $2.0, 2.5, 3.0$ , and  $3.2 \times 10^5$  K. (c) Ratio of predicted to observed brightness temperature, with contours of 1.2 (inner) and 1.5 (outer).

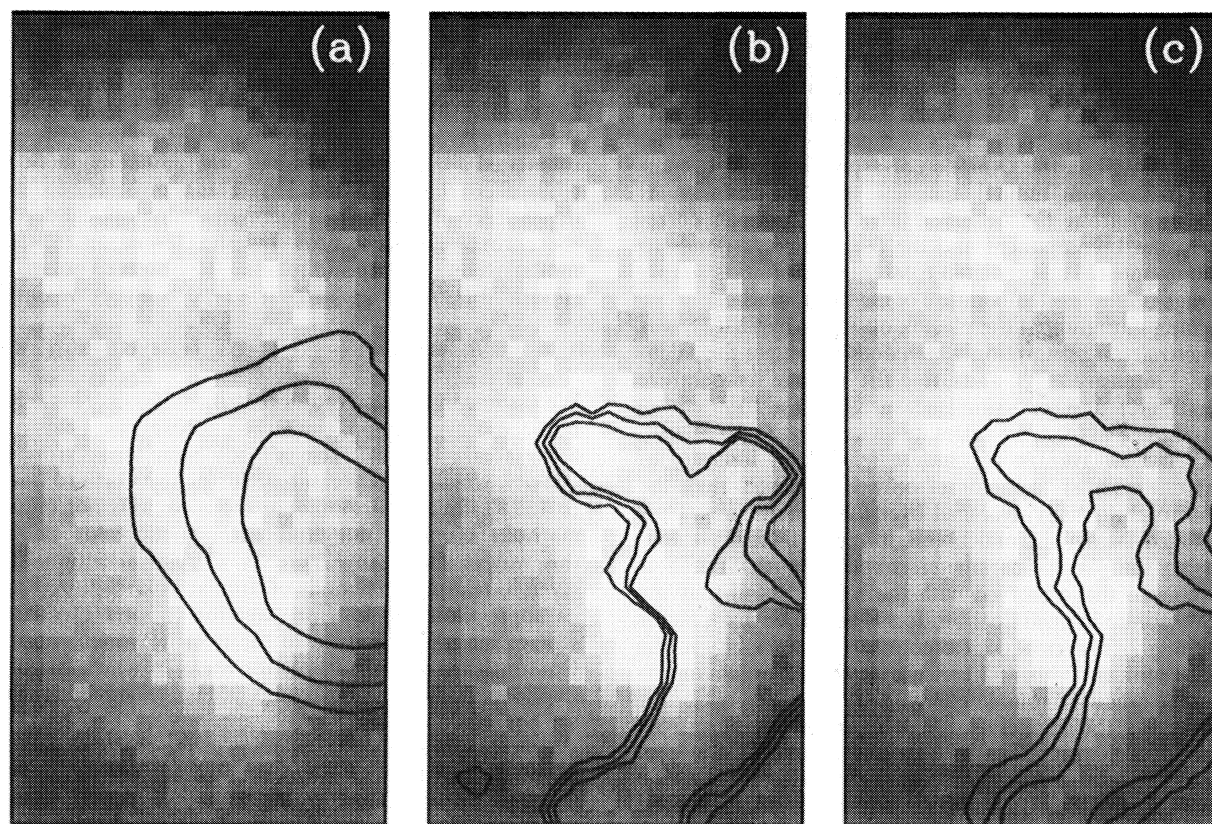


FIG. 5.—Contours of (a) the coronal longitudinal magnetic field calculated from the combined EUV and microwave polarization observations, (b) the coronal potential longitudinal field extrapolated to a height of 5000 km, and (c) the coronal potential longitudinal field extrapolated to a height of 10,000 km. Contour levels on all three figures are  $-30, -40$ , and  $-50$  G. The background image is that of Fe XVI at 335 Å in all three frames.



the same. Our calculated values of the coronal longitudinal field from the combined SERTS and VLA observations are very close to the extrapolated potential values. This suggests that the potential field extrapolation for this relatively weak region is fairly reliable and that the majority of the hot plasma observed by both SERTS and the VLA lies at heights of  $\sim 5000$ – $10,000$  km.

#### 4. CONCLUSIONS

We briefly summarize the main conclusions of this analysis:

1. The 20 cm microwave emission observed by the VLA can be adequately explained by thermal bremsstrahlung emission from the hot, magnetized plasma observed in the EUV by SERTS. The structure and intensity of the calculated and the observed maps are quite similar, indicating that neither absorption in a cool overlying layer nor emission from a gyroresonance layer is required. We have used the Meyer (1991, 1992) revised coronal iron abundance ( $1.33 \times 10^{-4}$ ), which is a factor of 3.4 greater than the Meyer (1985) coronal iron abundance.

2. The coronal longitudinal magnetic field is calculated by combining the observed 20 cm polarization obtained from the VLA with the plasma parameters obtained from SERTS. A map of the coronal magnetic field obtained in this way shows that the longitudinal magnetic field is  $\sim 30$ – $60$  G in the micro-

wave emission region. These values are comparable to values obtained using the Sakurai (1982) potential field extrapolation code for heights of 5000 and 10,000 km. This suggests that the magnetic field in this region is potential, and that the hot plasma observed by SERTS and the VLA lies at heights  $\sim 5000$ – $10,000$  km.

3. Maps of the electron temperature across the plage are obtained by taking ratios of the Fe xvi intensity maps at 335 and 361 Å to the Fe xv intensity map at 284 Å. These maps show that the electron temperature of the plasma to which Fe xvi/Fe xv is sensitive is  $2.5 \times 10^6$  K over most of the plage. The temperature reaches a maximum value of  $2.9 \times 10^6$  K where strong, oppositely directed magnetic polarities are closely spaced. The emission measure also attains its maximum value at this location.

4. A filament channel appears dark in the EUV because its column emission measure is lower than that in the adjacent plasma.

Research at Goddard Space Flight Center was supported in part by NASA RTOPs 170-38-53 and 879-11-38. Research at the University of Maryland was supported by NSF grant ATM 90-19893 and NASA grant NAGW-1541. NSO/Kitt Peak data used here are produced cooperatively by NSF/NOAO, NASA/GSFC, and NOAA/SEL.

#### REFERENCES

- Arnaud, M., & Raymond, J. 1992, *ApJ*, 398, 394  
 Brosius, J. W., & Holman, G. D. 1988, *ApJ*, 327, 417  
 ———. 1989, *ApJ*, 342, 1172  
 Brosius, J. W., Holman, G. D., & Schmelz, J. T. 1991, *Eos*, 72, 449  
 Brosius, J. W., Willson, R. F., Holman, G. D., & Schmelz, J. T. 1992, *ApJ*, 386, 347  
 Chiuderi-Drago, F., Bandiera, R., Falciani, R., Antonucci, E., Lang, K. R., Willson, R. F., Shibasaki, K., & Slottje, C. 1982, *Sol. Phys.*, 80, 71  
 Davila, J. M., Thomas, R. J., Thompson, W. T., Keski-Kuha, R. A. M., & Neupert, W. M. 1992, in *Proc. 10th Int. Conf. on UV and X-Ray Spectroscopy of Astrophysical and Laboratory Plasmas*  
 Fuhr, J. R., Martin, G. A., & Wiese, W. L. 1988, *J. Phys. Chem. Ref. Data*, 17, 1  
 Holman, G. D. 1986, in *Coronal and Prominence Plasmas*, ed. A. I. Poland (NASA CP-2442), 297  
 Holman, G. D., & Kundu, M. R. 1985, *ApJ*, 292, 291  
 Jones, H. P., Duvall, T. L., Jr., Harvey, J. W., Mahaffey, C. T., Schwitters, J. D., & Simmons, J. E. 1992, *Sol. Phys.*, 139, 211  
 Jordan, S. D., Thompson, W. T., Thomas, R. J., & Neupert, W. M. 1993, *ApJ*, 406, 346  
 Kanno, M., & Suematsu, Y. 1982, *PASJ*, 34, 449  
 Keski-Kuha, R. A. M., Thomas, R. J., & Davila, J. M. 1992, *Proc. SPIE*, 1546, 614  
 Kundu, M. R., Schmahl, E. J., & Gerassimenko, M. 1980, *A&A*, 82, 265  
 Kundu, M. R., Schmahl, E. J., & Rao, A. P. 1981, *A&A*, 94, 72  
 Landini, M., & Monsignori Fossi, B. C. 1990, *A&AS*, 82, 229  
 Lang, K. R. 1980, *Astrophysical Formulae* (New York: Springer-Verlag)  
 Lang, K. R., Willson, R. F., Smith, K. L., & Strong, K. T. 1987a, *ApJ*, 322, 1035  
 ———. 1987b, *ApJ*, 322, 1044  
 Mewe, R., Gronenschild, E. H. B. M., & van den Oord, G. H. J. 1985, *A&AS*, 62, 197  
 Meyer, J.-P. 1985, *ApJS*, 57, 173  
 Meyer, J.-P. 1991, *Adv. Space Res.*, 11, 269  
 ———. 1992, private communication  
 Neupert, W. M., Brosius, J. W., Thomas, R. J., & Thompson, W. T. 1992a, *ApJ*, 392, L95  
 Neupert, W. M., Epstein, G. L., Thomas, R. J., & Thompson, W. T. 1992b, *Sol. Phys.*, 137, 87  
 Neupert, W. M., & Kastner, S. O. 1983, *A&A*, 128, 188  
 Nitta, N., et al. 1991, *ApJ*, 374, 374  
 Pallavicini, R., Sakurai, T., & Vaiana, G. S. 1981, *A&A*, 98, 316  
 Pottasch, S. R. 1963, *ApJ*, 137, 945  
 ———. 1964, *Space Sci. Rev.*, 3, 816  
 Sakurai, T. 1982, *Sol. Phys.*, 76, 301  
 Schmahl, E. J., & Orrall, F. Q. 1979, *ApJ*, 231, L41  
 Schmelz, J. T., Holman, G. D., Brosius, J. W., & Gonzalez, R. D. 1992, *ApJ*, 399, 733  
 Shibasaki, K., Chiuderi-Drago, F., Melozzi, M., Slottje, C., & Antonucci, E. 1983, *Sol. Phys.*, 89, 307  
 Stern, R., Wang, E., & Bowyer, S. 1978, *ApJS*, 37, 195  
 Thomas, R. J., Keski-Kuha, R. A. M., Neupert, W. M., Condor, C. E., & Gum, J. S. 1991, *Appl. Opt.*, 30, 2245  
 Thomas, R. J., Neupert, W. M., & Thompson, W. T. 1992, *Proc. 10th Int. Conf. on UV and X-Ray Spectroscopy of Astrophysical and Laboratory Plasmas*  
 Thompson, W. T., Neupert, W. M., Jordan, S. D., Jones, H. P., Thomas, R. J., & Schmieder, B. 1993, *Sol. Phys.*, in press  
 Tousey, R., Bartoe, J.-D. F., Brueckner, G. E., & Purcell, J. D. 1977, *Appl. Opt.*, 16, 870  
 Webb, D. F., Davis, J. M., Kundu, M. R., & Velusamy, T. 1983, *Sol. Phys.*, 85, 267  
 Webb, D. F., Holman, G. D., Davis, J. M., Kundu, M. R., & Shevgaonkar, R. K. 1987, *ApJ*, 315, 716